Heliyon 9 (2023) e21189

Contents lists available at ScienceDirect

Heliyon

journal homepage: www.cell.com/heliyon

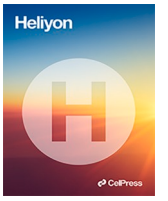

Impact of solid-fluid interfacial layer and nanoparticle diameter on Maxwell nanofluid flow subjected to variable thermal conductivity and uniform magnetic field

Pudhari Srilatha [a], R.S. Varun Kumar [b], R. Naveen Kumar [b], R.J. Punith Gowda [c], Amal Abdulrahman [d], B.C. Prasannakumara [e,*]

[a] Department of Mathematics, Institute of Aeronautical Engineering, Hyderabad, India
[b] Department of Mathematics, Amrita School of Engineering, Amrita Vishwa Vidyapeetham, Bengaluru, Karnataka, India
[c] Department of Mathematics, Bapuji Institute of Engineering & Technology, Davanagere, 577004, Karnataka, India
[d] Department of Chemistry, College of Science, King Khalid University, Abha, 61421, Saudi Arabia
[e] Department of Studies and Research in Mathematics, Davangere University, Shivagangotri, Davangere, 577002, Karnataka, India

ARTICLE INFO

Keywords:
Maxwell fluid
Uniform magnetic field
Heat source/sink
Disk
Nanofluid interfacial layer

ABSTRACT

The utilization of Maxwell fluid with nanoparticle suspension exhibits promising prospects in enhancing the efficacy of energy conversion and storage mechanisms. They have the potential to be utilized in sophisticated cooling systems for power generation facilities, thereby augmenting the overall energy efficacy. Keeping this in mind, the current research examines the Maxwell nanofluid flow over a rotating disk with the impact of a heat source/sink. The present study centers on the examination of flow characteristics in the existence of a uniform magnetic field. The conversion of governing equations into ordinary differential equations is achieved using appropriate similarity variables. To derive the Nusselt number (*Nu*) and skin friction (SF) model related to the flow and temperature parameters, the suggested back-propagation artificial neural networking (ANN) technique is used. The Runge-Kutta-Fehlberg fourth-fifth order (RKF-45) method is used to solve the reduced equations and produce the necessary data to create the *Nu* and SF model. Both the *Nu* and SF models require 1000 data for training the network, respectively. Graphs are utilized to communicate numerical outcomes. The results concluded that the upsurge in magnetic parameter drops the velocity profile but advances the heat transport. Rise in the thermal conductivity parameter, increases the heat transport.

1. Introduction

The flow of fluids with variable thermal conductivity is a phenomenon that may occur in a variety of natural and manufactured systems. This occurs when the thermal conductivity of the liquid varies as a temperature function which can be seen in heat exchangers. This phenomenon may take place in a wide variety of fluids, including gases and liquids, and is an important factor to take into account in a number of different industrial and environmental processes. The substance capacity to transport heat is quantified by a property known as its thermal conductivity. This quality changes with temperature in liquids that have a variable thermal

* Corresponding author.
E-mail addresses: pudhari.srilatha@gmail.com (P. Srilatha), varursv@gmail.com (R.S.V. Kumar), nkrmaths@gmail.com (R.N. Kumar), rjpunithgowda@gmail.com (R.J.P. Gowda), Amlsaad@kku.edu.sa (A. Abdulrahman), dr.bcprasanna@gmail.com (B.C. Prasannakumara).

https://doi.org/10.1016/j.heliyon.2023.e21189
Received 25 June 2023; Received in revised form 15 October 2023; Accepted 18 October 2023
Available online 23 October 2023

Nomenclature

E	Electric field
η	Dimensionless similarity coordinate
J	Current density
M	Magnetic parameter
Q	Heat source/sink parameter
λ_1	Relaxation time
T_∞	Ambient temperature
δ	Thermal conductivity parameter
β	Deborah number
$\theta(\eta)$	Dimensionless thermal profile
α	angle between the horizontal magnetic field components
τ_1	Heat diffusion relaxation time
k	Thermal conductivity
ν	Dynamic viscosity
$F(\eta), G(\eta), H(\eta)$	Non-dimensional velocity profiles
Re	Local Reynolds number
ρC_p	Heat capacitance
B	Magnetic field strength
σ	Magnetic conductivity
Q_0	Heat source/sink coefficient
Ω	Angular disk speed
$P(\eta)$	Dimensionless pressure
T	Temperature
d	Nanoparticle diameter
μ	Dynamic viscosity
(r, φ, z)	Directions
M	Magnetic parameter
(u, v, w)	Velocity components
Sc	Schmidt number

Subscript

Pr	Prandtl number
f	Fluid
ω	Stretching parameter
nf	Nanofluid
ρ	Density
s	Solid nanoparticle

Abbreviations

NF	Nanofluid
NNF	Non-Newtonian fluid
MF	Maxwell fluid
UMF	Uniform magnetic field
HSS	Heat source/sink
Nu	Nusselt number
SF	Skin friction
NPs	Nanoparticles

conductivity; as a result, temperature may have a substantial effect on the way of liquids flow and the rates at which heat is transferred. Hayat et al. [1] explored the mixed convective stream of a liquid by considering variable thermal conductivity. Recently, Afridi et al. [2] and Afridi et al. [3] explored the stream of different NFs with varied physical conditions by considering variable thermal conductivity features. Qasim and Afridi [4] and Qasim et al. [5] swotted the stream of a variety NFs under a variety of various physical circumstances by taking into consideration of the properties of varying thermal conductivity.

The NFs are distinguished from conventional fluids by their possession of a distinct set of characteristics. NFs often exhibit improved thermophysical characteristics as a result of the presence of nanoparticles (NPs). Because of these properties, NFs are becoming more appealing for use in various applications requiring heat transmission and thermal control. The suspension of graphene NPs in sodium alginate is considered in this study. The examination of the flow of NF using graphene NPs suspensions has shown some

exciting new paths for the development of creative technological applications. Edward C. Stanford, a British pharmacist, made the first discovery of sodium alginate in 1881 (see Refs. [6,7]). Contrary to more traditional solvent-based methods, sodium alginate has been particularly employed for the aqueous microencapsulation of pharmaceuticals formulations (see Refs. [8,9]). Recently, Adnan [10] explored the heat transfer in different NPs over a Riga surface. Alharbi and Adnan [11] swotted the heat transfer in different alumina NPs. Recently, Adnan et al. [12–14] examined the influence of different features of different NPs in the suspension of various base liquids.

The interaction of the NPs with the base liquid results in the formation of the interfacial layers. An interfacial layer develops around each NPs as a consequence of interactions among the surrounding liquid molecules and the scattered NPs. This layer is made up of a mixture of molecules from the base fluid and the NP surface. There are numerous significant ramifications for nanofluids of the creation of interfacial layers. The stability of NFs dispersion is first affected by these layers. By forming a barrier that stops the nanoparticles from congregating or settling, the interfacial layers may provide steric stability. This improves the nanofluid's long-term stability and enables it to keep its well-dispersed condition. The flow of ferrofluid past a spinning disk with solid–liquid interfacial layer was evaluated by Acharya [15]. The flow of NF with the impact of inducing novel effects was probed by Adnan and Ashraf [16]. The influence of solid–fluid interfacial layer on the NF stream past a needle was analyzed by Shafiq et al. [17]. The convective flow of a NF past a needle with the interfacial layer and shape impacts was probed by Shaw et al. [18]. Gowda et al. [19] scrutinized the influence of an interfacial layer on the stream of NF over a stretchy surface.

Depending on the physical properties of liquids they are classified as Newtonian or non-Newtonian fluid (NNF) types. An NNF has variable viscosity that varies with stress. Many salt solutions and molten polymers are NNFs, as are several commonplace items such as shampoo, starch suspensions, melted butter, blood, corn starch, toothpaste, paint, and custard. NNFs have many uses in manufacturing and engineering fields like adhesives, drilling muds, nuclear reactors, metal spinning, and plastic polymers. A single model cannot describe all of the features of these liquids. As a consequence, several models of non-Newtonian have been created to describe the characteristics and behavior of these liquids. These models are characterized into three types: rate fluids, integrals, and differentials. The MF model is identified as a kind of rate-type liquid. Furthermore, unlike differential-type liquids, this model defines the relaxation time impact. Shah et al. [20] scrutinized the flow of MF via a permeable cone. MF flow past a shrinking geometry was inspected by Shi et al. [21]. The MF stream past a plate was examined by Fetecau et al. [22] using mathematical analysis. Soret–Dufour effects on the MF flow via an exponential stretchy sheet were deliberated by Abbas et al. [23]. The stream of MF past a surface was deliberated by Kumar and Reddy [24] with chemical reaction.

Magnetic fields are used in the investigation of geothermal reservoirs, generators, petroleum reservoirs, accelerators, pumps, magnetic filtration and separation, microfluidic devices, and flow meters. The magnetohydrodynamic flow of NNF in particular is of great interest in magnetotherapy. In fact, a great deal of investigation has been done to inspect the behavior of magnetic fields in a variety of configurations. Magnetized fluid flows can also help with medicine administration in a variety of disorders. One strategy involves the binding of pharmaceuticals to physiologically suitable magnetic particles, which leads to the target via the precise and proper positioning of permanent magnetic particles on the body's external surface. A uniform magnetic field (UMF) is one which has the same magnitude as well as direction across the region, therefore the field lines should be simultaneously parallel and equally spaced. Galerkin finite element scheme was applied by Adnan and Ashraf [25] to investigate the thermal features of NF with magnetic field. NF flow amid two inclined cylinders in the occurrence of a UMF was discussed by Pordanjani and Aghakhani [26]. Prasannakumara and Gowda [27] investigated the fluid passing across a disc in existence of a UMF. The NF flow across a disk with the influence of a UMF was probed by Wang et al. [28]. Turkyilmazoglu [29] scrutinized the impact of a UMF on the liquid stream past a porous channel.

The influence of heat source/sink (HSS) is quite beneficial to the industry. For example, the excellence of the finished product greatly depends on the heat management component. Many elements were considered by researchers/scholars while analyzing the significance of HSS on the dynamics of NL flow with heat transport capabilities. Kumar et al. [30] considered the NL flow via a disk in the existence of an HSS. The power-law liquid flow via a spinning disk in the existence of non-uniform HSS was explored by Usman et al. [31]. Roy and Pop [32] educed the stream of NF past a sheet with the HSS. Effects of HSS on NF stream over a surface were probed by Adnan et al. [33]. Song et al. [34] scrutinized the Williamson liquid stream past a surface with a HSS.

Considering the several practical uses in engineering fields such as electronic devices, rotating machinery, gas air cleaning machines, thermal-power generating systems, crystal growth processes, turbine rotors, medical equipment, and computer storage devices, researchers continue to pay close attention to the heat transport problem over a rotating disk. Heat transmission analysis and fluid flow via a disk with the upshot of a magnetic field were carried out by Ahmad et al. [35]. Shehzad et al. [36] scrutinized the liquid stream past a disk utilizing the effects of Soret-Dufour. The stream of Sutterby liquid due to a disk was considered by Mabood et al. [37] utilizing a heat flux model. The consequence of the magnetic field was used by Rauf et al. [38] to scrutinize the flow of hybrid ferrofluid past a disk. Numerical simulation was employed by Sharma et al. [39] to examine the fluid properties and NL flow via a rotating disk.

The majority of research has concentrated on NFs, even though many have looked at the behavior of NFs in different convection modes. There isn't much information available on impact of UMF and HSS on Maxwell NFs that include graphene NPs suspended in sodium alginate. Complex fluid dynamics and heat transfer phenomena may be produced by the interactions of graphene NPs suspension in sodium alginate, which have not been completely investigated. As a result, there is a research gap in the full study of sodium alginate-based NF flow and heat transfer considering the UMF and variable thermal conductivity phenomena. To fill this research gap, present research intends to increase knowledge of various aspects and their influence on the flow and thermal features of Maxwell NF, laying the groundwork for future developments in the field.

2. Formulation of a problem

The present study examines the fluid dynamics of a Maxwell nanofluid (sodium alginate and graphene) flow that is generated by a stretching rotating disk. The scenario involves the application of a uniform external magnetic field, denoted as B, to a disk that is undergoing rotation around its axial axis z at a consistent angular velocity represented by Ω. The present study assumes an axisymmetric induced velocity field denoted by u = (u, v, w), accompanied by pressure p and temperature T. The system is presumed to exhibit azimuthal coordinate symmetry with respect to φ, while the disk is considered to be infinitely extensive in the radial direction r. The representation of the uniform magnetic field in the cylindrical coordinate system can be expressed in vector form, as $B = (B_r, B_\varphi, B_z)$ according to Turkyilmazoglu [40]. The Lorentz force is able to be broken down into its constituent parts and represented by the following equation, which can be found in Turkyilmazoglu [40].

$$J \times B = \sigma\left(-B_\varphi(B_\varphi u - B_r v),\ -B_r(B_\varphi u - B_r v),\ -\left(B_\varphi^2 + B_r^2\right)w\right). \tag{1}$$

The aforementioned flow assumptions give rise to the subsequent flow model and adopting Equation (1) following governing equations can be obtained (see refs. Acharya [15], Wang et al. [28] and Turkyilmazoglu [40]):

$$\frac{1}{r}\frac{\partial}{\partial r}(r\,u) + \frac{\partial w}{\partial z} = 0, \tag{2}$$

$$\begin{aligned} u\frac{\partial u}{\partial r} + w\frac{\partial u}{\partial z} - \frac{v^2}{r} &= -\frac{1}{\rho_{nf}}\frac{\partial p}{\partial r} + \nu_{nf}\left(\frac{\partial^2 u}{\partial r^2} + \frac{1}{r}\frac{\partial u}{\partial r} + \frac{\partial^2 u}{\partial z^2} - \frac{u}{r^2}\right) \\ -\lambda_1\left(\begin{array}{l} u^2\frac{\partial^2 u}{\partial r^2} + w^2\frac{\partial^2 u}{\partial z^2} + 2u\,w\frac{\partial^2 u}{\partial r \partial z} + \frac{u\,v^2}{r^2} \\ -\frac{2u\,v}{r}\frac{\partial v}{\partial r} - \frac{2v\,w}{r}\frac{\partial v}{\partial z} + \frac{v^2}{r}\frac{\partial u}{\partial r} \end{array}\right) &+ \frac{\sigma_{nf}}{\rho_{nf}}\left(-B_\varphi(B_\varphi u - B_r v)\right) \end{aligned} \tag{3}$$

$$\begin{aligned} u\frac{\partial v}{\partial r} + w\frac{\partial v}{\partial z} + \frac{u\,v}{r} &= \nu_{nf}\left(\frac{\partial^2 v}{\partial r^2} + \frac{1}{r}\frac{\partial v}{\partial r} + \frac{\partial^2 v}{\partial z^2} - \frac{v}{r^2}\right) \\ -\lambda_1\left(\begin{array}{l} u^2\frac{\partial^2 v}{\partial r^2} + w^2\frac{\partial^2 v}{\partial z^2} + 2u\,w\frac{\partial^2 v}{\partial r \partial z} - \frac{2v\,u^2}{r^2} \\ +\frac{2u\,v}{r}\frac{\partial u}{\partial r} + \frac{2v\,w}{r}\frac{\partial u}{\partial z} - \frac{v^3}{r^2} + \frac{v^2}{r}\frac{\partial v}{\partial r} \end{array}\right) &+ \frac{\sigma_{nf}}{\rho_{nf}}\left(B_r(B_\varphi u - B_r v)\right) \end{aligned} \tag{4}$$

$$\begin{aligned} u\frac{\partial w}{\partial r} + w\frac{\partial w}{\partial z} &= -\frac{1}{\rho_{nf}}\frac{\partial p}{\partial z} + \nu_{nf}\left(\frac{\partial^2 w}{\partial r^2} + \frac{1}{r}\frac{\partial w}{\partial r} + \frac{\partial^2 w}{\partial z^2}\right) \\ -\lambda_1\left(u^2\frac{\partial^2 w}{\partial r^2} + 2u\,w\frac{\partial^2 w}{\partial r \partial z} + w^2\frac{\partial^2 w}{\partial z^2} + \frac{v^2}{r}\frac{\partial w}{\partial r}\right) &+ \frac{\sigma_{nf}}{\rho_{nf}}\left(-\left(B_\varphi^2 + B_r^2\right)w\right) \end{aligned} \tag{5}$$

$$\begin{aligned} \left(u\frac{\partial T}{\partial r} + w\frac{\partial T}{\partial z}\right) &= \frac{1}{\left(\rho c_p\right)_{nf}}\left(\frac{k_{nf}(T)}{r}\frac{\partial T}{\partial r} + \frac{\partial}{\partial r}\left(k_{nf}(T)\frac{\partial T}{\partial r}\right) + \frac{\partial}{\partial z}\left(k_{nf}(T)\frac{\partial T}{\partial z}\right)\right) \\ -\tau_1\left(\begin{array}{l} u\frac{\partial u}{\partial r}\frac{\partial T}{\partial r} + w\frac{\partial w}{\partial z}\frac{\partial T}{\partial z} + u\frac{\partial w}{\partial r}\frac{\partial T}{\partial z} + w\frac{\partial u}{\partial z}\frac{\partial T}{\partial r} \\ +2u\,w\frac{\partial^2 T}{\partial r \partial z} + u^2\frac{\partial^2 T}{\partial r^2} + w^2\frac{\partial^2 T}{\partial z^2} \end{array}\right) &+ \frac{Q_0}{\left(\rho c_p\right)_{nf}}(T - T_\infty) \end{aligned} \tag{6}$$

following appropriate boundary constraints have been established for the assumed flow problem (see refs. Acharya [15], Wang et al. [28] and Turkyilmazoglu [40]):

$$\begin{aligned} &u(0) = sr, v(0) = \Omega r, w(0) = 0, T(0) = T_w \ \ at\ \ z = 0 \\ &u \to 0, v \to 0, T \to T_\infty, p \to 0, as \quad z \to \infty \end{aligned} \tag{7}$$

If the inclination angle between the direction of the magnetic field vector $B = (B_r, B_\varphi, 0)$ and the r-direction is given as α (see Turkyilmazoglu [40]).

$$(B_\varphi, B_r = |B|(\sin\alpha, \cos\alpha)). \tag{8}$$

The subsequent similarity transformations are hereby presented as follows (see refs. Acharya [15], Wang et al. [28] and Turkyilmazoglu [40]):

$$\left.\begin{aligned}&\eta = z\left(\frac{\Omega}{\nu}\right)^{\frac{1}{2}}, p(\eta) = \left(\rho_f \nu_f\ \Omega\ P(\eta)\right), w = (\Omega\ \nu)^{\frac{1}{2}} H(\eta),\\ &\theta(\eta) = \frac{T - T_\infty}{T_w - T_\infty}, v = r\ \Omega\ G(\eta), u = r\ \Omega\ F(\eta), k_{nf}(T) = k_{nf}\left(1 + \delta\frac{T - T_\infty}{T_w - T_\infty}\right).\end{aligned}\right\} \tag{9}$$

Furthermore, the thermophysical feature of NFs are given by (Xue et al. [41])

$$\mu_{nf} = \mu_f\left(\frac{1}{(1-\varphi)^{2.5}}\right), \tag{10}$$

$$\rho_{nf} = (1-\varphi)\rho_f + \varphi\rho_s, \tag{11}$$

$$(\rho C_p)_{nf} = (1-\varphi)(C_p\rho)_f + \varphi(C_p\rho)_s. \tag{12}$$

The traditional correlations for thermal conductivity, as postulated by Hamilton and Crosser [42], were not applied in this investigation as they failed to adequately characterize the notably increased thermal conductivity detected in NFs. The primary cause of this intrinsic susceptibility stems from the lack of consideration given by conventional models to the molecular solid-liquid interface layer or NP diameter when calculating thermal conductivity correlations. The interfacial layer among the solid-fluid phases and the NP diameter are critical determinants in the detected rise in thermal conductivity. The subsequent correlations for modified thermal conductivity are given Murshed et al. [43] and Leong et al. [44]:

$$k_{nf} = k_f\frac{\left(1-\gamma_2^3+2\gamma_1^3\right)\varphi\beta_1\left(k_s - k_f\beta_1\right) + \gamma_1^3\left\{\beta_1 - 1\right\}\varphi\gamma_2^3 + 1\right)\left(k_s + 2k_f\beta_1\right)}{\left(k_s + 2k_f\beta_1\right)\gamma_1^3 - \left(k_s - k_f\beta_1\right)\varphi(\gamma_2^3 - 1 + \gamma_1^3)}, \tag{13}$$

with

$\left(h, \gamma_1, \gamma_2 = \sigma_l\sqrt{2\pi}, 1 + \frac{h}{d}\frac{1}{2}, 1 + \frac{h}{d}\right)$, where $d = 10$ and $\sigma_l = [0.2 - 0.8]\ nm$. Also, for $\sigma_l = 0.4nm$ we have $h \approx 1nm$ based on refs. [45, 46]

Now the governing Equations (2)–(6) can be transformed, by utilizing Equation (8), similarity transformations Equation (9), and the thermophysical feature of NFs Equations 10–13 as follow:

$$H' + 2F = 0 \tag{14}$$

$$\begin{aligned}&\frac{\nu_{nf}}{\nu_f}F'' - F^2 + G^2 - HF' - \beta\left(H^2F'' + 2FF'H - 2HGG'\right)\\ &\quad -\frac{\rho_f}{\rho_{nf}}\left(M\sin^2(\alpha)F - M\sin(\alpha)\cos(\alpha)G\right) = 0\end{aligned} \tag{15}$$

$$\begin{aligned}&\frac{\nu_{nf}}{\nu_f}G'' - 2FG - HG' - \beta\left(H^2G'' + 2FG'H + 2HGF'\right)\\ &\quad + \left(\frac{\rho_f}{\rho_{nf}}M\cos(\alpha)\sin(\alpha)F - \frac{\rho_f}{\rho_{nf}}M\cos^2(\alpha)G\right) = 0\end{aligned} \tag{16}$$

$$\frac{\rho_f}{\rho_{nf}}P' = -\frac{\nu_{nf}}{\nu_f}2F' + \beta\left(2H^2F'\right) + 2HF - \frac{\rho_f}{\rho_{nf}}MH \tag{17}$$

$$\frac{\left(\rho c_p\right)_f}{\left(\rho c_p\right)_{nf}}\frac{k_{nf}}{k_f}\left[(1+\delta\theta)\theta'' + \delta(\theta')^2\right] - \Pr H\theta' - \gamma\Pr\left(HH'\theta' + H^2\theta''\right) + \frac{\left(\rho c_p\right)_f}{\left(\rho c_p\right)_{nf}}\Pr Q\theta = 0 \tag{18}$$

the boundary constraints have been reduced to:

$$\begin{aligned}&\eta = 0 : F = \omega, G = 1, H = 0, \theta = 1\\ &\eta\to\infty : F = \theta = P = G\to 0\end{aligned} \tag{19}$$

where,

$$\beta = \lambda_1\Omega, M = \frac{\sigma_{nf}|B|^2}{\rho_f\Omega}, \Pr = \frac{\left(\mu C_p\right)_f}{k_f}, Q = \frac{Q_0}{\left(\rho C_p\right)_f\Omega}, \gamma = \tau_1\Omega, \omega = \frac{s}{\Omega}.$$

Skin friction and Nusselt number for the assumed flow are as follow:

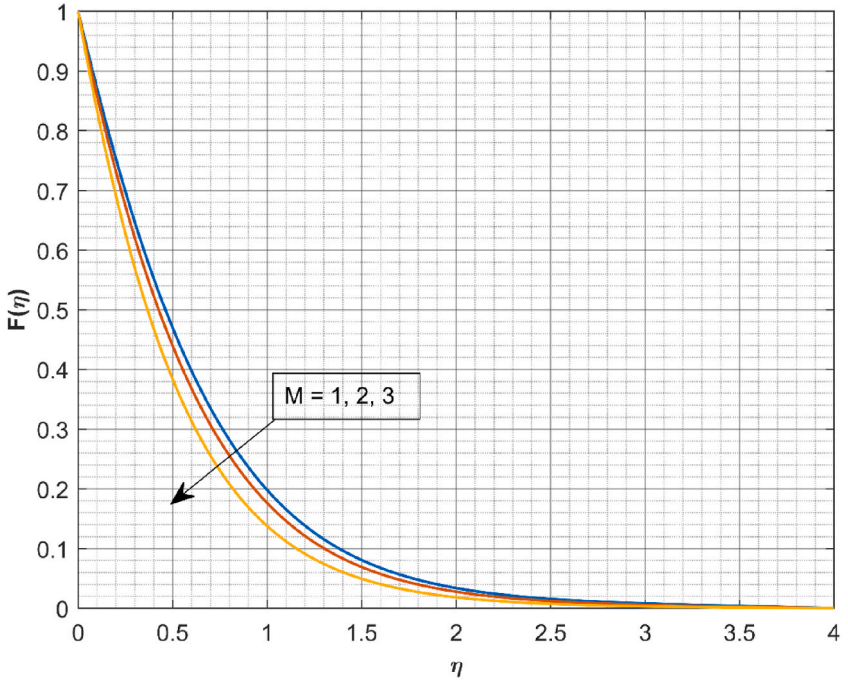

Fig. 1. Consequence of M on $F(\eta)$.

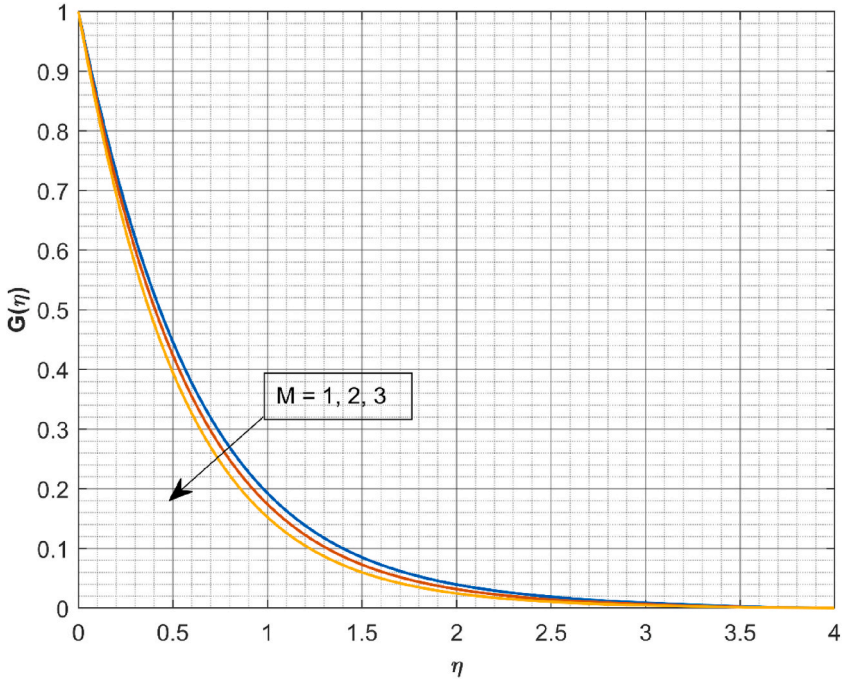

Fig. 2. Consequence of M on $G(\eta)$.

$$\mathrm{Re}^{1/2}\mathrm{C}_f = \sqrt{\left(\left[\frac{\mu_{nf}}{\mu_f}\right]^2 G'(0)\right)^2 + \left(\left[\frac{\mu_{nf}}{\mu_f}\right]^2 F'(0)\right)^2} \tag{20}$$

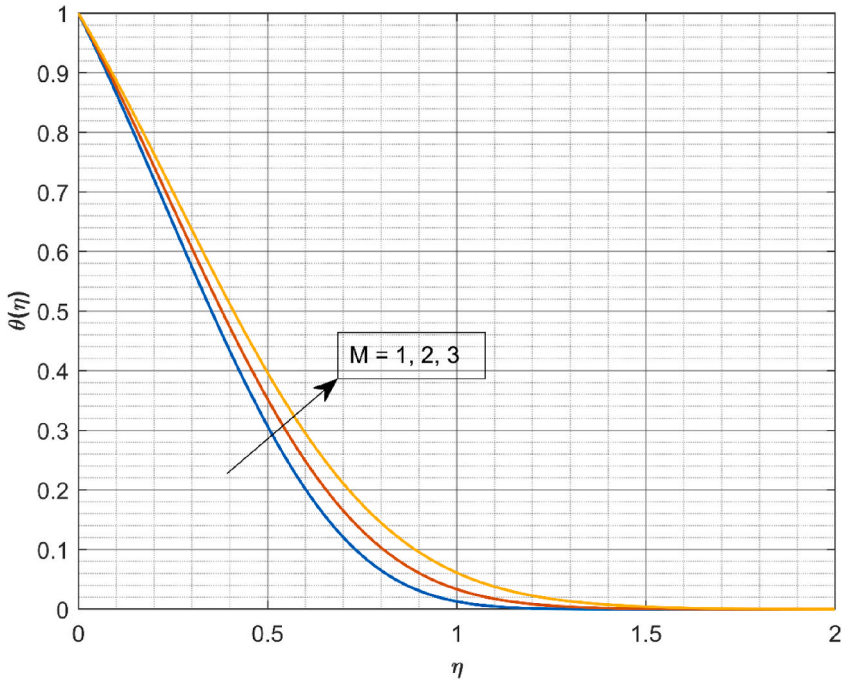

Fig. 3. Consequence of M on $\theta(\eta)$.

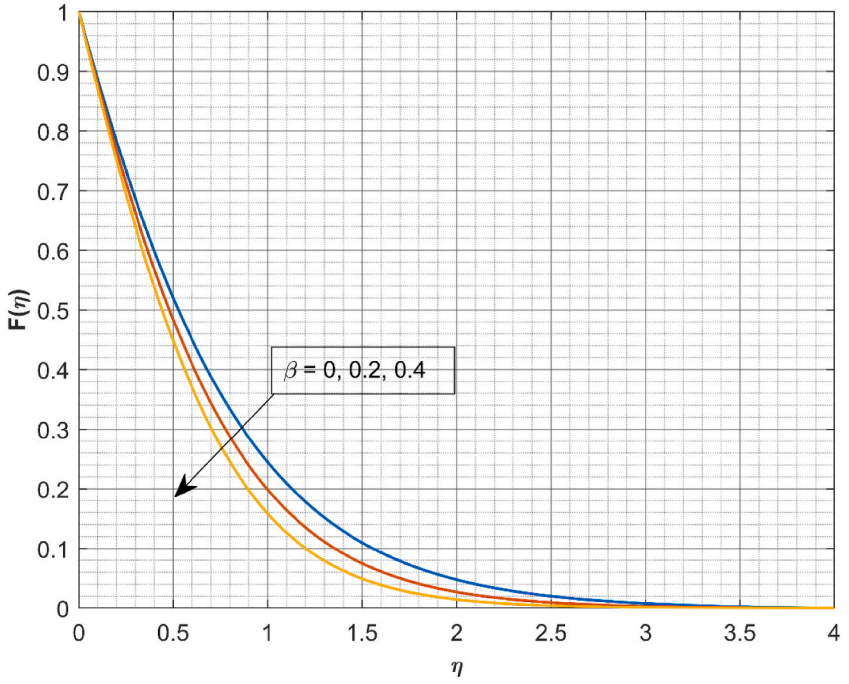

Fig. 4. Consequence of β on $F(\eta)$.

$$\mathrm{Re}^{-1/2}Nu = -\frac{k_{inf}}{k_f}\theta'(0). \tag{21}$$

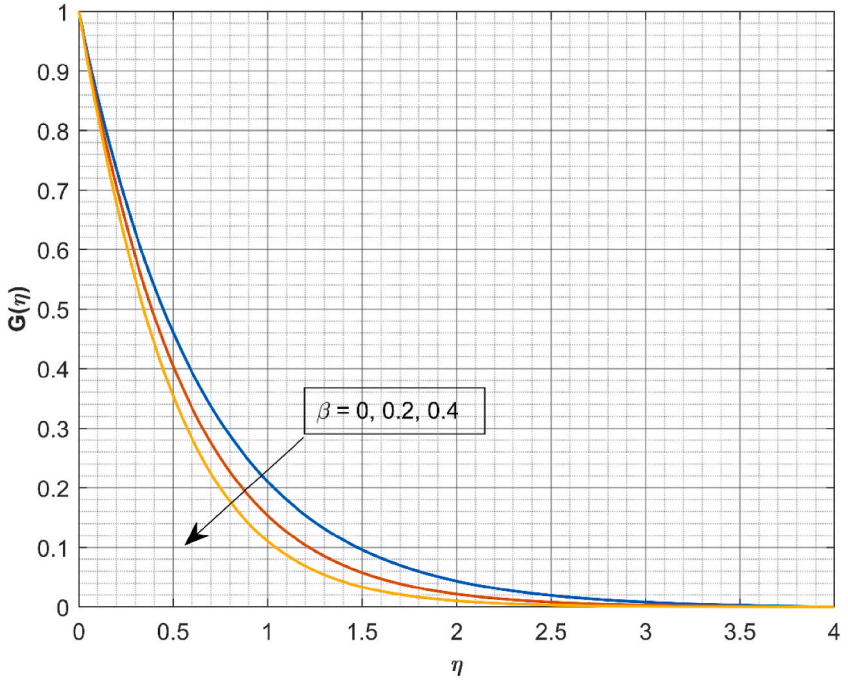

Fig. 5. Consequence of β on $G(\eta)$.

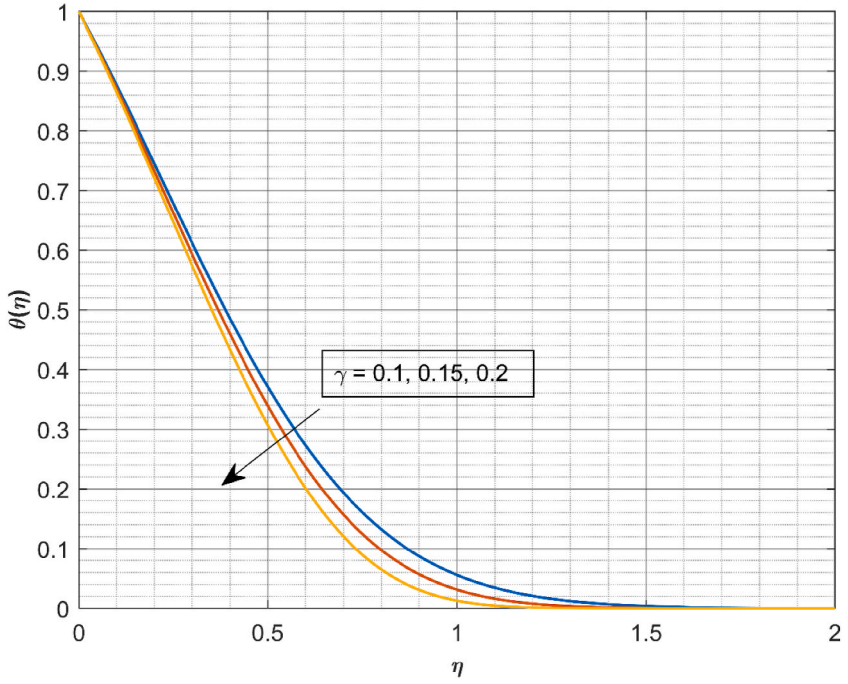

Fig. 6. Consequence of γ on $\theta(\eta)$.

3. Results and discussion

This section elaborates on the significant research results. The set of PDEs (2)–(6) and the boundary conditions (7) are reduced into the ODEs (14)–(18) along with boundary conditions Equation (19). The physical quantities Skin friction and Nusselt number for the assumed flow can be studied by using Equations 20 and 21. The flow behaviours on velocity and heat transport are described

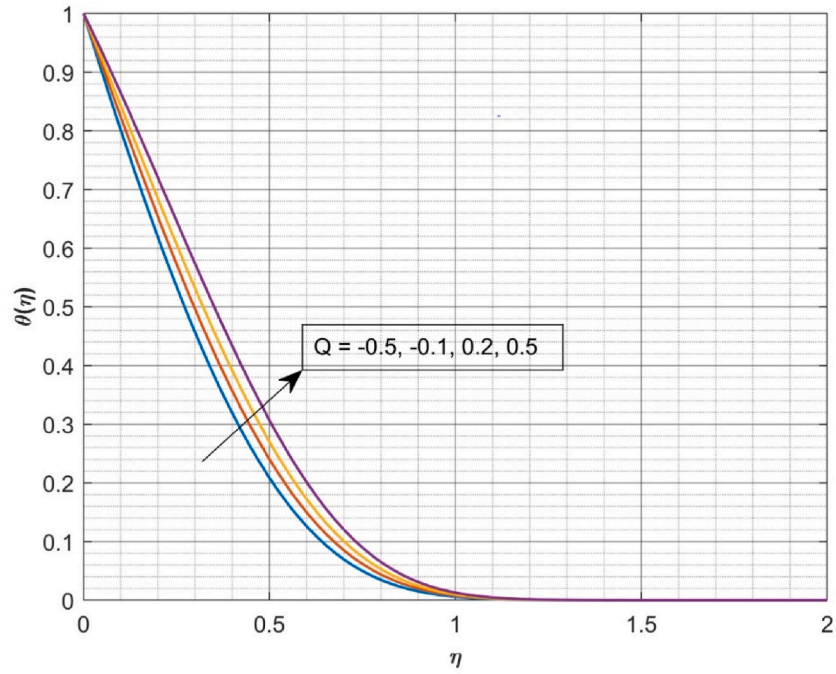

Fig. 7. Consequence of Q on $\theta(\eta)$.

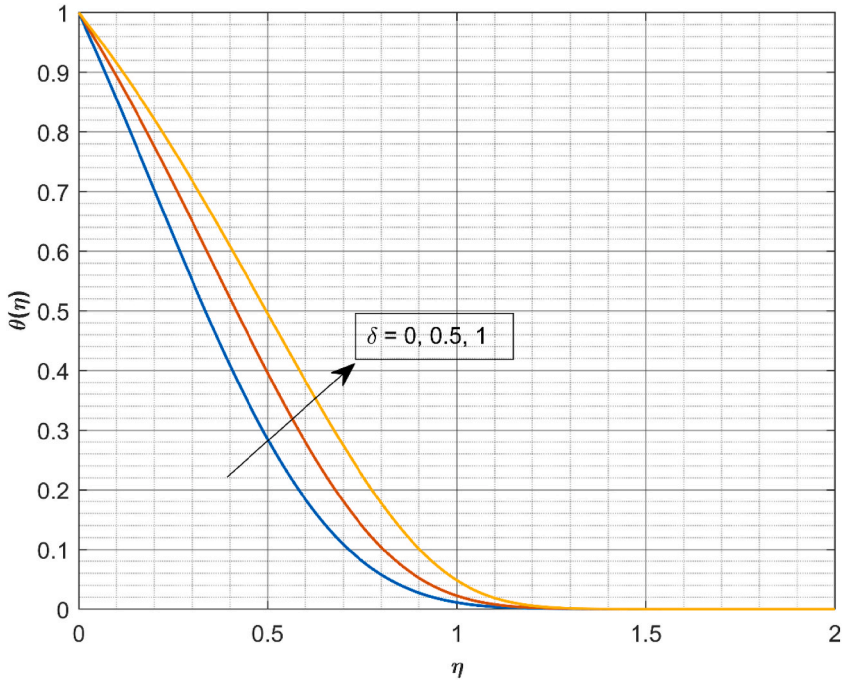

Fig. 8. Consequence of δ on $\theta(\eta)$.

numerically for various parameters, and the results are graphically depicted in Figs. 1–9. ANN models are used to depict engineering coefficients such as drag force and heat transport rate. The outcomes of the developed ANN models are indicated through the performance metrics. In the calculation the static values of the parameters are considered in the range as follow $M = [0.1 - 4]$, $\beta = [0 - 1]$, $\gamma = [0.1 - 1]$, $Q = [-1, 1]$, $\delta = [0, 1]$ unless otherwise specified. Table 1 presents the thermophysical features of base liquid and NPs. We compared numerical findings to available work in Table 2. The results show excellent matching, which gives us validation of

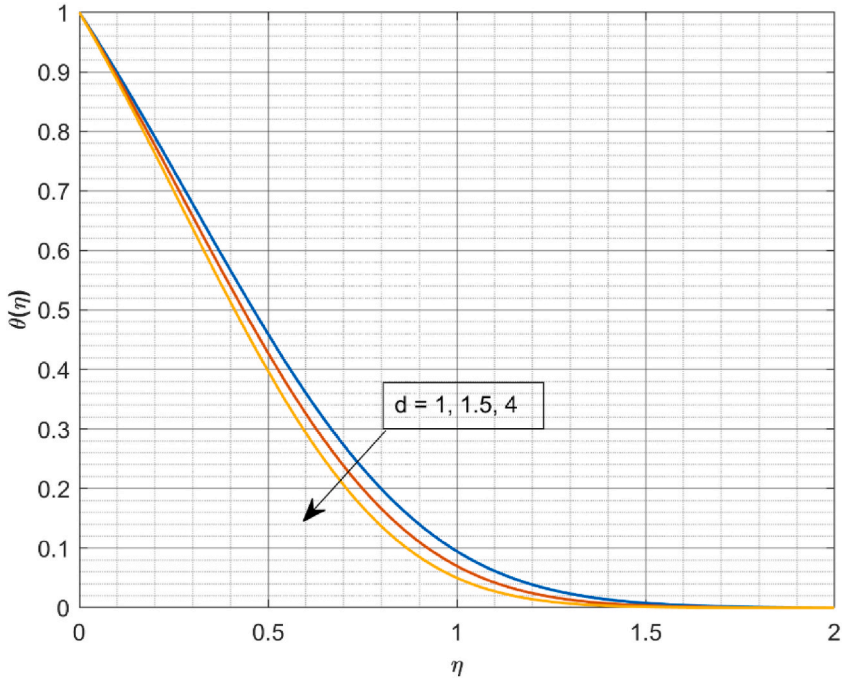

Fig. 9. Consequence of d on $\theta(\eta)$.

Table 1
Exploration of thermophysical characteristics of base and nanoparticle (refs. [8,9,47,48]).

Physical features	$c_p(J/kg\,K)$	$\rho(kg/m^3)$	$k(W/mk)$	Pr
Graphene	2100	2250	2500	–
NaA lg	4175	989	0.6376	6.5

Table 2
Comparison of the, $F^{'}(0)$ and $-\theta^{'}(0)$ values for some reduced cases.

	$F^{'}(0)$	$-\theta^{'}(0)$
Ref. [49]	0.510233	–
Ref. [50]	0.5102	0.9337
Ref. [51]	0.51023262	0.93387794
Present results	0.51023264	0.93387795

the current study.

Figs. 1 and 2 portrays the impact of M on $F(\eta)$ and $G(\eta)$. With the rise in M (1, 2, 3), both velocities are decreased. Physically, the Lorentz force is a resistive force that opposes motion which is created when magnetic lines of force engage with an electrically conducting fluid in motion. This opposing force causes the reduction in velocity profiles. The nature of $\theta(\eta)$ with the influence of M is revealed in Fig. 3. The value of magnetic interaction paramater increases, $\theta(\eta)$ rises simultaneously. The Lorentz force is a resistive force that physically resists motion. It is created when magnetic lines of force contact with moving electrically conducting fluid as a result $\theta(\eta)$ increases. As the values of Deborah number β upsurges (0, 0.2, 0.4), both velocities $F(\eta)$ and $G(\eta)$ are decreased as it is shown in Figs. 4 and 5. Deborah number is related to a relaxation time. The relaxation time increases as β increases, resulting in increased resistance among fluid layers due to this the velocity curves $F(\eta)$ and $G(\eta)$, establish a decreasing nature in relation to the Deborah number. Fig. 6 exhibits the upshot of γ on thermal profile. As rise in γ (0.1, 0.15, 0.2), reduces the heat transport. The thermal field is reduced as relaxation time increases. Fluid molecules transfer energy to nearby molecules more slowly as their relaxation time rises. Therefore, the temperature curves show a declining nature or behaviour. The influence of Q on $\theta(\eta)$ was shown in Fig. 7. As a result of the augmented fluid temperatures, the thermal boundary layer extends, as the Q increases. When the strength of a heat sink is increased, the gradient in wall temperature rises, but a heat source displays the opposite tendency. The consequence of δ on the $\theta(\eta)$ is presented in Fig. 8. Rise in the δ increases the $\theta(\eta)$. It is important to note that when molecules collide, energy is transferred, which raises the temperature. As a result, an upsurge in the δ leads to an improvement in temperature of fluid as well as an enhancement of

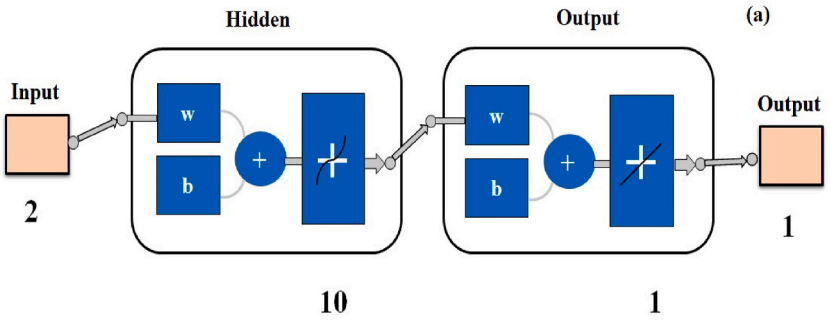

Fig. 10. ANN design for Nusselt number.

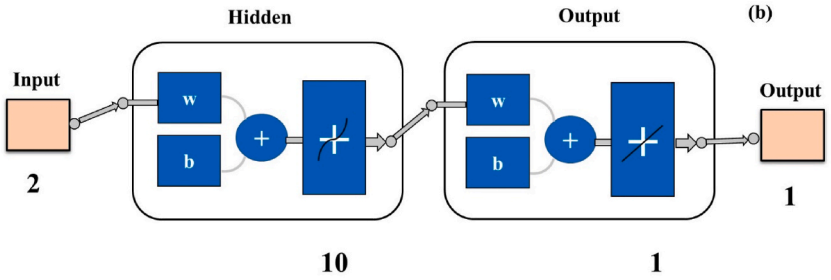

Fig. 11. ANN design for skin friction.

$\theta(\eta)$. The outcome of d on $\theta(\eta)$ is depicted in Fig. 9. NPs characterized by reduced diameters exhibit heightened thermal conductivity and improved Brownian motion when compared to their larger counterparts. Consequently, only NPs with reduced dimensions demonstrate relatively lower temperature measurements.

4. ANN architecture

The most powerful approach to artificial intelligence is known as artificial neural network (ANN), and it was created to solve technical problems while drawing inspiration from the way the human brain works. The system is composed of linked neurons that serve as fundamental operating units for obtaining and combining signals. In terms set out by the brain system, the data is sent from neuron to neuron by an association or a weight. While there are other ANN configurations, including the radial basis function neural network (RBFNN), autoencoder, convolutional neural network (CNN), etc., the multilayer perceptron (MLP) is the most often used network for dealing with nonlinear issues. Pre-processed input data are fed into the network by the input layer (IL). The first layer's inputs are connected to the hidden layer (HL), which is made up of different transfer functions that are comparable to biological neurons. A basic MLP typically has one layer in which the number of neurons is optimized, even if the hidden layer may have several layers of neurons. One or more functions that generate predictions for the process model are included in the output layer (OL).

To derive the *Nu* and SF model related to the flow and temperature parameters, the suggested back-propagation ANN technique is used. The RKF-45 technique is utilized to solve the non-dimensional flow and thermal equation and produce the necessary data to create the *Nu* and SF model. Both the *Nu* and SF models require 1000 data for training, correspondingly.

For the performance evaluation of the created MLP network model, MSE and Determination Coefficient (R) metrics were employed. Below are the formulae used to calculate performance parameters.

$$MSE = \frac{1}{\mathrm{K}} \sum_{i=1}^{\mathrm{K}} \left(\vartheta_{\exp(j)} - \vartheta_{ANN(j)}\right)^2$$

$$R^2 = 1 - \frac{\sum_{j=1}^{\mathrm{K}} \left(\vartheta_{\exp(j)} - \vartheta_{ANN(j)}\right)^2}{\sum_{j=1}^{\mathrm{K}} \left(\vartheta_{\exp(j)}\right)^2}$$

$$Error\ \ rate(\%) = \left[\frac{\vartheta_{\exp} - \vartheta_{ANN}}{\vartheta_{\exp}}\right] \times 100$$

Two inputs and ten hidden neurons are pondered in the *Nu* and SF models, correspondingly. Figs. 10 and 11 signifies the IL, HL, and

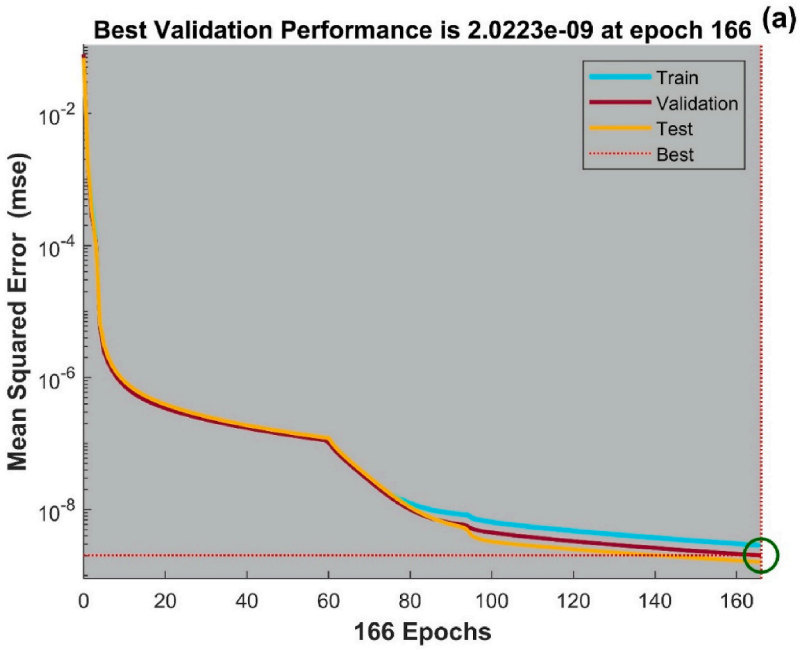

a. Performance of the ANN for Nusselt number.

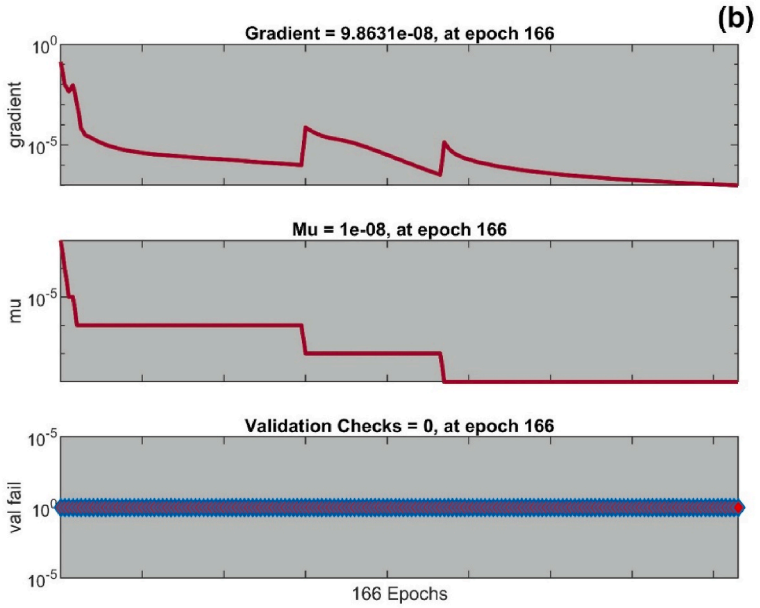

b. The Gradient, Mu, and validation check for Nusselt number.

Fig. 12. a) Performance of the ANN for Nusselt number. (b) The Gradient, Mu, and validation check for Nusselt number. (c) Regression plot for the Nusselt number. (d) Error histogram result for Nusselt number.

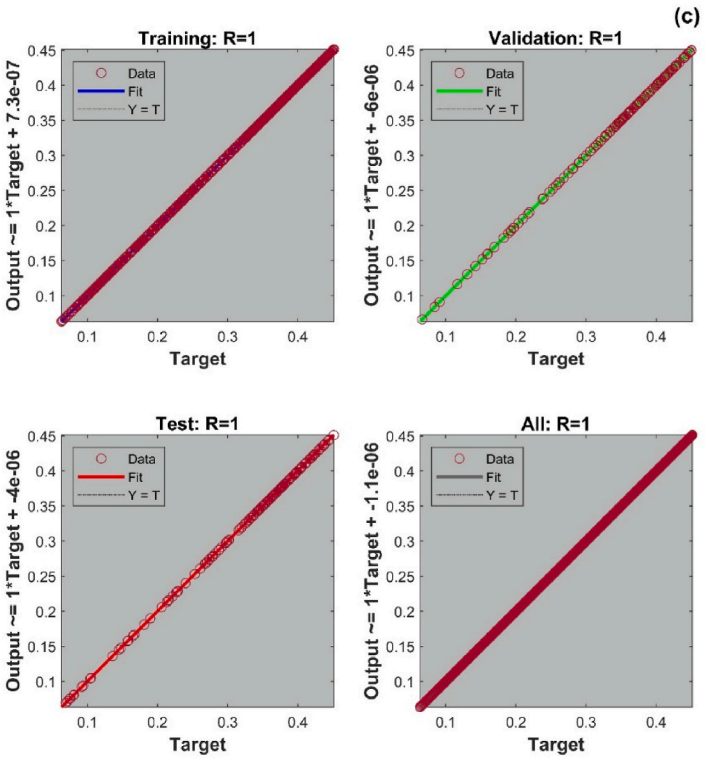

c. Regression plot for the Nusselt number.

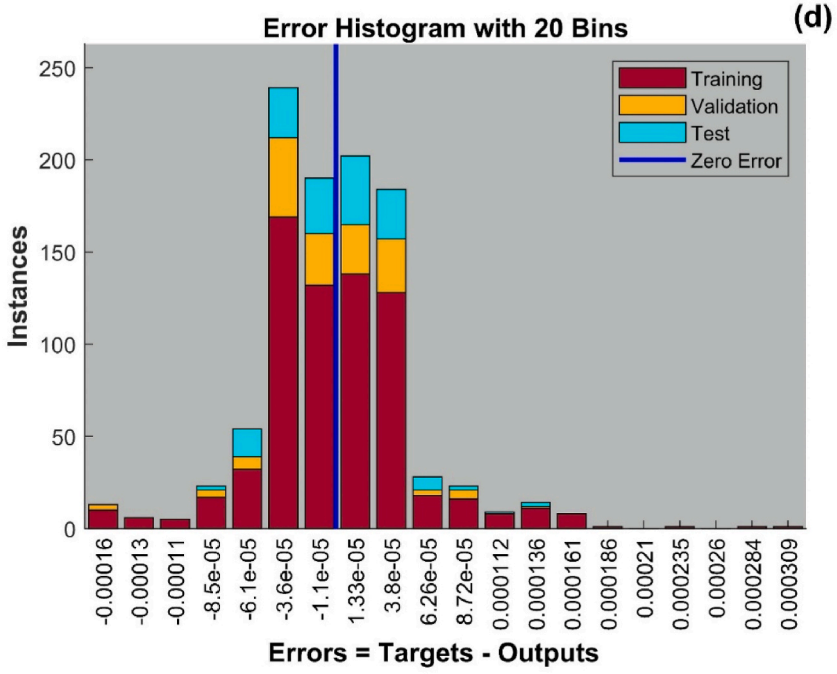

d. Error histogram result for Nusselt number.

Fig. 12. (*continued*).

OLs of the trained ANN for *Nu* and SF models respectively.

Figs. 12a and 13a present the optimal ANN performance for the *Nu* and SF models respectively. The average of the square of error divided by the total number of data points is estimated by the MSE of any solution approach. A lower MSE for any computational

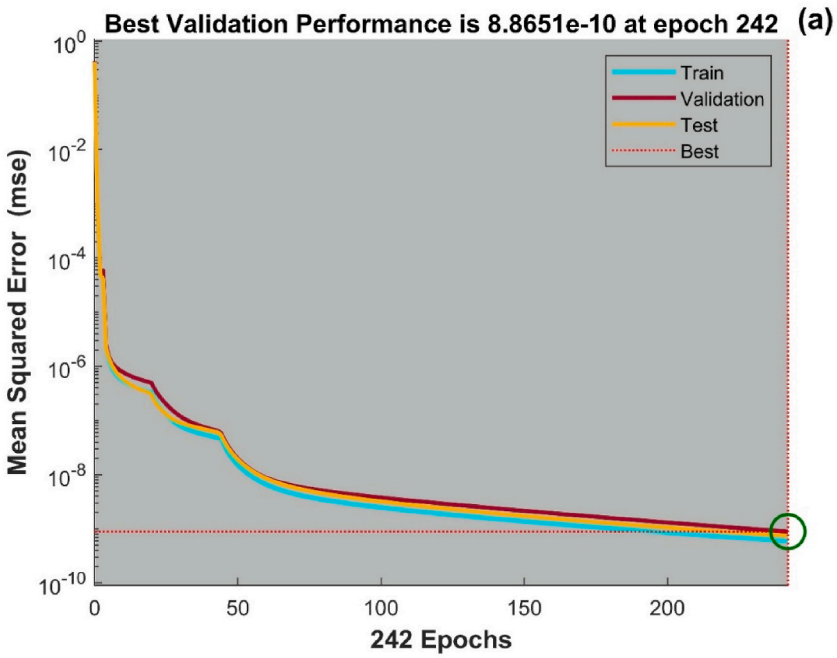

a. Performance of the ANN for skin friction.

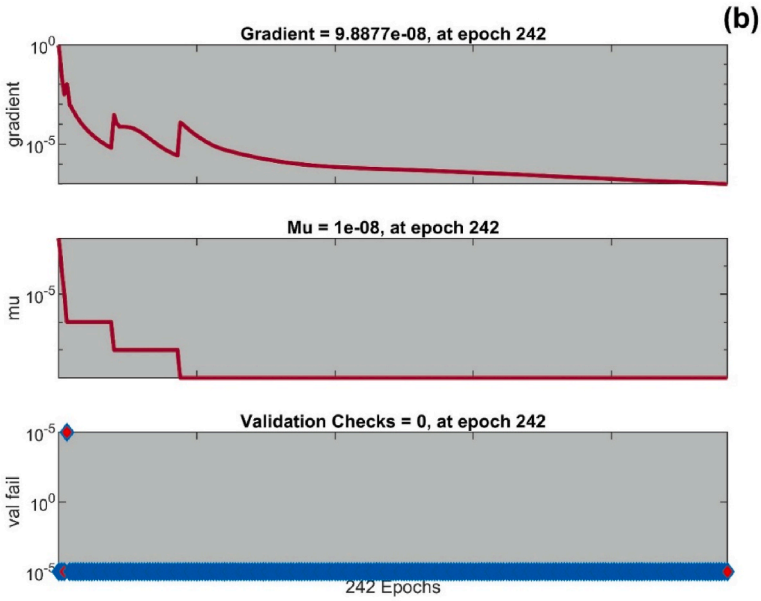

b. The Gradient, Mu, and validation check for skin friction.

Fig. 13. a) Performance of the ANN for skin friction. (b) The Gradient, Mu, and validation check for skin friction. (c) Regression plot for the skin friction. (d) Error histogram result for skin friction.

approach indicates improved accuracy, performance, and solution stability. A magnitude of 2.0223×10^{-9} is attained as lowest finest MSE performance for *Nu* at epoch 166. Further, at epoch 242, the trained SF model exhibits the ideal MSE of 8.8651×10^{-10}.

Figs. 12b and 13b exemplify the verification of the ANN by means of validation check regarding the *Nu* and SF respectively. The

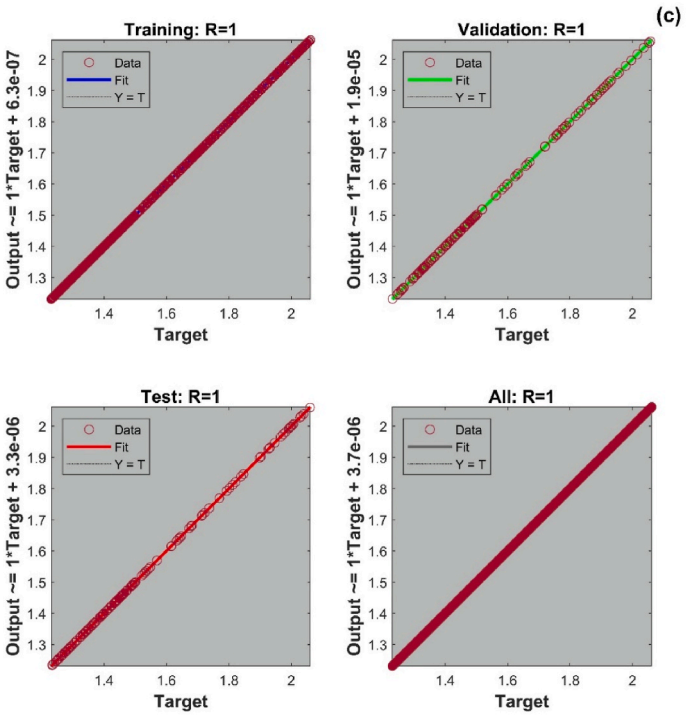

c. Regression plot for the skin friction.

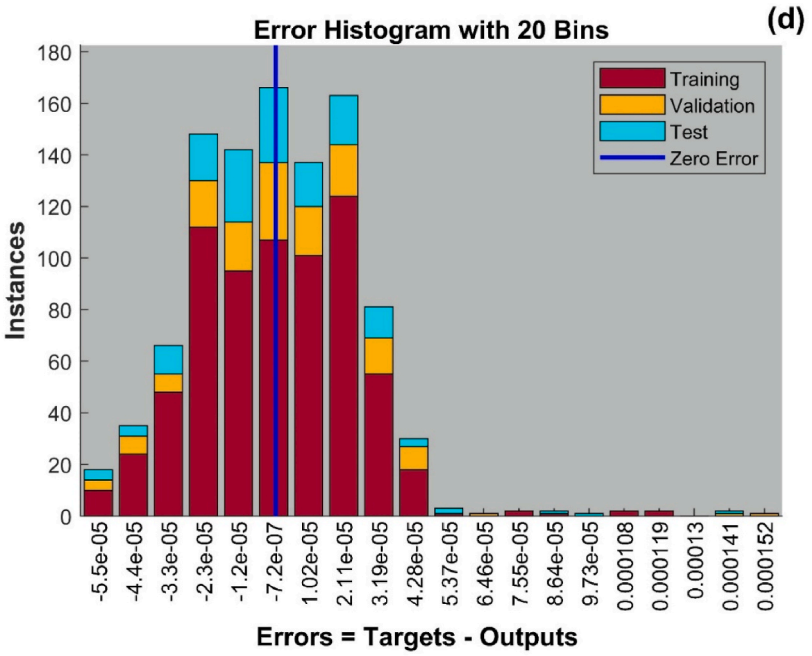

d. Error histogram result for skin friction.

Fig. 13. (*continued*).

Table 3
ANN results for the *Nu* with error estimation.

Q	γ	Nu_{num}	Nu_{ANN}	$ABS(error)$
0	0.1	0.42591366	0.425858441	5.52×10^{-5}
0.14		0.30764729	0.307617089	3.02×10^{-5}
0.21		0.23858831	0.238602493	1.42×10^{-5}
0.28		0.15908765	0.159094998	7.35×10^{-6}
0.35		0.06312651	0.063175139	4.86×10^{-5}
0.1	0	0.32488727	0.32481673	7.05×10^{-5}
	0.05	0.33399366	0.333995773	2.11×10^{-6}
	0.10	0.34371449	0.343714435	5.54×10^{-8}
	0.15	0.35409432	0.354117913	2.36×10^{-5}
	0.20	0.36518412	0.365162904	2.12×10^{-5}

Table 4
ANN results for the C_f with error estimation.

M	β	$C_{f_{num}}$	$C_{f_{ANN}}$	$ABS(error)$
0	0.1	1.247137	1.247257462	0.000120462
0.1		1.2912382	1.29120247	3.57×10^{-5}
0.2		1.3351238	1.335178565	5.48×10^{-5}
0.3		1.3787387	1.378716744	2.20×10^{-5}
0.4		1.4220404	1.421994569	4.58×10^{-5}
0.5		1.4649967	1.465007225	1.05×10^{-5}
0.5	0	1.4981372	1.498134971	2.23×10^{-6}
	0.12	1.4579596	1.45796023	6.30×10^{-7}
	0.15	1.4471311	1.447125825	5.28×10^{-6}
	0.18	1.4359626	1.435967209	4.61×10^{-6}
	0.21	1.4244385	1.424453321	1.48×10^{-5}

gradient, which is calculated during the training of the network is some form of vector with a defined magnitude and direction. To update the suggested network in a precise direction and with an exact value, the gradient vector is used. The employed algorithm during the network's training is controlled by the parameter mu. Mu's value has a direct impact on how quickly the solution converges. The gradient value for the *Nu* is 9.8631×10^{-8} achieved at epoch 166 as shown in Fig. 12b, and the equivalent Mu scale is 1×10^{-8} acquired at epoch 166. For the SF model, Fig. 13b shows the values 9.8877×10^{-8} and 1×10^{-8} for the gradient and Mu at epoch 242.

The regression plots for *Nu* and SF are shown in Figs. 12c and 13c respectively. The predictive capability of the training algorithm is determined using correlation coefficients by evaluating the forecasted sample points to the regression line. The value of R extremely near to 1 demonstrates how well the operated model calculation matches the original results. By observing Figs. 12c and 13c, Correlation coefficient values are consistently around unity, i.e. $R = 1$, which is the ideal value for training, testing, and validation of perfect modeling. The trained value is therefore obtained with the lowest possible error for both the *Nu* and SF.

Figs. 12d and 13d illustrate the error distribution of developed ANN simulations for *Nu* and SF respectively with the influence of various parameters. The errors dispersal from the reference line is shown by the error histogram. The quantity of values from each data set that are contained in a given bin is shown in each bar of the figure. For *Nu* and SF models, the zero error is achieved at the value -1.1×10^{-5} and -7.2×10^{-7} respectively.

Table 3 shows the ANN results for the Nusselt number with parameters Q and γ and also it indicates the error estimation between the data of the numerical values and ANN. Upon observing Table 3, the closer convergence between the numerical and ANN results is obtained with maximum error 7.05×10^{-5} and minimum error 5.54×10^{-8}. The performed ANN results indicate the closer convergence with the numerical results with training, validation and testing performance of 2.91×10^{-10}, 2.66×10^{-10} and 2.94×10^{-10} respectively.

The ANN results for the skin friction with parameters M and β are tabulated in Table 4. It also shows the error estimation between the results of the numerical values and ANN. With maximum error 0.000120462 and minimum error 6.30×10^{-7}, the closer convergence is achieved between the numerical and ANN outcomes. With training, validation, and testing performance of 4.19×10^{-10}, 4.74×10^{-10} and 4.48×10^{-10} respectively, the ANN results show a closer convergence with the numerical findings.

5. Conclusion

This article aims to investigate the flow of a Maxwell NF on a rotating stretching disk with HSS. The focus of the current enquiry pertains to the analysis of flow properties with homogeneous external magnetic field. The process of transforming non-linear governing equations into ordinary differential equations is accomplished by utilizing suitable similarity variables. The numerical solution of the reduced equations is obtained by employing a shooting method and utilizing the RKF-45 order method. Visual aids such as graphs and charts are employed to effectually convey numerical results. The outcomes concluded that the rise in M declines the ve-

locity profile but improves the heat transport. The relaxation time increases as β increases, resulting in increased resistance among fluid layers due to this the velocity curves $F(\eta)$ and $G(\eta)$ decreases. Rise in the δ, increases the $\theta(\eta)$. Furthermore, the NPs with smaller diameters exhibit comparatively lower temperature readings. For *Nu* and SF models, the zero error is achieved at the value -1.1×10^{-5} and -7.2×10^{-7} respectively. The performed ANN results indicate the closer convergence with the numerical results with training, validation and testing performance of 2.91×10^{-10}, 2.66×10^{-10} and 2.94×10^{-10} respectively.

Data availability statement

Data will be made available on request.

Additional information

No additional information is available for this paper.

CRediT authorship contribution statement

Pudhari Srilatha: Formal analysis, Investigation. **R.S. Varun Kumar:** Conceptualization, Investigation, Writing – original draft. **R. Naveen Kumar:** Methodology, Validation, Writing – original draft. **R.J. Punith Gowda:** Formal analysis, Software, Writing – original draft. **Amal Abdulrahman:** Formal analysis, Methodology. **B.C. Prasannakumara:** Conceptualization, Investigation, Supervision.

Declaration of competing interest

The authors declare that they have no known competing financial interests or personal relationships that could have appeared to influence the work reported in this paper.

Acknowledgement

The author would like to extend his appreciation to the Deanship of Scientific Research at King Khalid University, Saudi Arabia for funding this work through the Research Group Program under grant No. RGP.2/218/44.

References

[1] T. Hayat, S.A. Shehzad, M. Qasim, A. Alsaedi, Mixed convection flow by a porous sheet with variable thermal conductivity and convective boundary condition, Braz. J. Chem. Eng. 31 (Mar. 2014) 109–117, https://doi.org/10.1590/S0104-66322014000100011.
[2] M.I. Afridi, M. Qasim, O.D. Makinde, Second law analysis of boundary layer flow with variable fluid properties, J. Heat Tran. 139 (104505) (Jun. 2017), https://doi.org/10.1115/1.4036645.
[3] M.I. Afridi, A. Wakif, M. Qasim, A. Hussanan, Irreversibility analysis of dissipative fluid flow over A curved surface stimulated by variable thermal conductivity and uniform magnetic field: utilization of generalized differential quadrature method, Entropy 20 (12) (Dec. 2018), https://doi.org/10.3390/e20120943, 12, Art.
[4] M. Qasim, M.I. Afridi, Effects of energy dissipation and variable thermal conductivity on entropy generation rate in mixed convection flow, J. Therm. Sci. Eng. Appl. 10 (Mar. 2018), 044501, https://doi.org/10.1115/1.4038703.
[5] M. Qasim, N. Riaz, D. Lu, M.I. Afridi, Flow over a needle moving in a stream of dissipative fluid having variable viscosity and thermal conductivity, Arabian J. Sci. Eng. 46 (8) (Aug. 2021) 7295–7302, https://doi.org/10.1007/s13369-021-05352-w.
[6] E. Stanford, Manufacture of Useful Products from Seaweeds, 1881. Great Britain.
[7] E.C. Stanford, 'On algin, a new substance obtained from some of the commoner species of marine algae, Am. J. Pharm. 47 (Dec. 1883) 617.
[8] F.A. Alwawi, H.T. Alkasasbeh, A.M. Rashad, R. Idris, MHD natural convection of Sodium Alginate Casson nanofluid over a solid sphere, Results Phys. 16 (Mar. 2020), 102818, https://doi.org/10.1016/j.rinp.2019.102818.
[9] T.N. Ahmed, I. Khan, Mixed convection flow of sodium alginate (SA-NaAlg) based molybdenum disulphide (MoS2) nanofluids: Maxwell Garnetts and Brinkman models, Results Phys. 8 (Mar. 2018) 752–757, https://doi.org/10.1016/j.rinp.2018.01.004.
[10] Adnan, Heat transfer inspection in [(ZnO-MWCNTs)/water-EG(50:50)]HNF with thermal radiation ray and convective condition over a Riga surface, Waves Random Complex Media (Sep. 2022) 1–15, https://doi.org/10.1080/17455030.2022.2119300.
[11] K.A.M. Alharbi, Adnan, Thermal investigation and physiochemical interaction of H2O and C2H6O2 saturated by Al2O3 and γAl2O3 nanomaterials, J. Appl. Biomater. Funct. Mater. 20 (Jan. 2022), 22808000221136484, https://doi.org/10.1177/22808000221136483.
[12] Adnan, et al., Applied heat transfer modeling in conventional hybrid (Al2O3-CuO)/C2H6O2 and modified-hybrid nanofluids (Al2O3-CuO-Fe3O4)/C2H6O2 between slippery channel by using least square method (LSM), AIMS Math 8 (math-08–02-215) (2023), 2, Art.
[13] K. Adnan, M. Abdulkhaliq, Alharbi, M.Z. Bani-Fwaz, S.M. Eldin, M.F. Yassen, Numerical heat performance of TiO2/Glycerin under nanoparticles aggregation and nonlinear radiative heat flux in dilating/squeezing channel, Case Stud. Therm. Eng. 41 (Jan. 2023), 102568, https://doi.org/10.1016/j.csite.2022.102568.
[14] Adnan, M. M AlBaidani, N. Kumar Mishra, Z. Ahmad, S. M Eldin, E. Ul Haq, Numerical study of thermal enhancement in ZnO-SAE50 nanolubricant over a spherical magnetized surface influenced by Newtonian heating and thermal radiation, Case Stud. Therm. Eng. 45 (May 2023), 102917, https://doi.org/10.1016/j.csite.2023.102917.
[15] N. Acharya, Framing the impacts of highly oscillating magnetic field on the ferrofluid flow over a spinning disk considering nanoparticle diameter and solid–liquid interfacial layer, J. Heat Tran. 142 (2020), https://doi.org/10.1115/1.4047503.
[16] Adnan, W. Ashraf, Numerical thermal featuring in γAl2O3-C2H6O2 nanofluid under the influence of thermal radiation and convective heat condition by inducing novel effects of effective Prandtl number model (EPNM), Adv. Mech. Eng. 14 (6) (Jun. 2022), 16878132221106576, https://doi.org/10.1177/16878132221106577.
[17] A. Shafiq, A.B. Çolak, T. Naz Sindhu, Designing artificial neural network of nanoparticle diameter and solid–fluid interfacial layer on single-walled carbon nanotubes/ethylene glycol nanofluid flow on thin slendering needles, Int. J. Numer. Methods Fluid. 93 (2021) 3384–3404, https://doi.org/10.1002/fld.5038.
[18] S. Shaw, A. Patra, A. Misra, M.K. Nayak, Assisting/opposing/forced convection flow on entropy-optimized MHD nanofluids with variable viscosity: interfacial layer and shape effects, Heat Transfer 51 (2022) 578–603, https://doi.org/10.1002/htj.22320.

[19] R.J.P. Gowda, R.N. Kumar, U. Khan, B.C. Prasannakumara, A. Zaib, A. Ishak, A.M. Galal, Dynamics of nanoparticle diameter and interfacial layer on flow of non-Newtonian (Jeffrey) nanofluid over a convective curved stretching sheet, Int. J. Mod. Phys. B 36 (2022), 2250224, https://doi.org/10.1142/S0217979222502241.

[20] Z. Shah, E. Alzahrani, M. Jawad, U. Khan, Microstructure and inertial characteristics of MHD suspended SWCNTs and MWCNTs based Maxwell nanofluid flow with bio-convection and entropy generation past a permeable vertical cone, Coatings 10 (2020) 998, https://doi.org/10.3390/coatings10100998.

[21] Q.-H. Shi, B. Ahmed, S. Ahmad, S.U. Khan, K. Sultan, M.N. Bashir, M.I. Khan, N.A. Shah, J.D. Chung, Dual solution framework for mixed convection flow of Maxwell nanofluid instigated by exponentially shrinking surface with thermal radiation, Sci. Rep. 11 (2021), 15944, https://doi.org/10.1038/s41598-021-95548-9.

[22] C. Fetecau, R. Ellahi, S.M. Sait, Mathematical analysis of Maxwell fluid flow through a porous plate channel induced by a constantly accelerating or oscillating wall, Mathematics 9 (2021) 90, https://doi.org/10.3390/math9010090.

[23] N. Abbas, W. Shatanawi, T.A.M. Shatnawi, Transportation of nanomaterial Maxwell fluid flow with thermal slip under the effect of Soret–Dufour and second-order slips: nonlinear stretching, Sci. Rep. 13 (2023) 2182, https://doi.org/10.1038/s41598-022-25600-9.

[24] M.A. Kumar, Y.D. Reddy, Computational modelling of radiative Maxwell fluid flow over a stretching sheet containing nanoparticles with chemical reaction, J. Indian Chem. Soc. 100 (2023), 100877, https://doi.org/10.1016/j.jics.2022.100877.

[25] Adnan, W. Ashraf, Thermal efficiency in hybrid (Al2O3-CuO/H2O) and ternary hybrid nanofluids (Al2O3-CuO-Cu/H2O) by considering the novel effects of imposed magnetic field and convective heat condition, Waves Random Complex Media (Jul. 2022) 1–16, https://doi.org/10.1080/17455030.2022.2092233.

[26] A.H. Pordanjani, S. Aghakhani, Numerical investigation of natural convection and irreversibilities between two inclined concentric cylinders in presence of uniform magnetic field and radiation, Heat Tran. Eng. 43 (2022) 937–957, https://doi.org/10.1080/01457632.2021.1919973.

[27] B.C. Prasannakumara, R.J.P. Gowda, Heat and mass transfer analysis of radiative fluid flow under the influence of uniform horizontal magnetic field and thermophoretic particle deposition, Waves in Random and Complex Media (2022) 1–12, https://doi.org/10.1080/17455030.2022.2096943.

[28] F. Wang, R.N. Kumar, B.C. Prasannakumara, U. Khan, A. Zaib, A.-H. Abdel-Aty, I.S. Yahia, M.S. Alqahtani, A.M. Galal, Aspects of uniform horizontal magnetic field and nanoparticle aggregation in the flow of nanofluid with melting heat transfer, Nanomaterials 12 (2022) 1000, https://doi.org/10.3390/nano12061000.

[29] M. Turkyilmazoglu, Uniform magnetic field impact on absolute versus convective onset of Darcy-Benard convection with horizontal throughflow, in: Review, 2023, https://doi.org/10.21203/rs.3.rs-2419665/v1.

[30] R. Naveen Kumar, H.B. Mallikarjuna, N. Tigalappa, R.J. Punith Gowda, D. Umrao Sarwe, Carbon nanotubes suspended dusty nanofluid flow over stretching porous rotating disk with non-uniform heat source/sink, Int. J. Comput. Methods Eng. Sci. Mech. 23 (2022) 119–128, https://doi.org/10.1080/15502287.2021.1920645.

[31] P. Lin Usman, A. Ghaffari, Steady flow and heat transfer of the power-law fluid between two stretchable rotating disks with non-uniform heat source/sink, J. Therm. Anal. Calorim. 146 (2021) 1735–1749, https://doi.org/10.1007/s10973-020-10142-x.

[32] N.C. Roy, I. Pop, Dual solutions of magnetohydrodynamic mixed convection flow of an Oldroyd-B nanofluid over a shrinking sheet with heat source/sink, Alex. Eng. J. 61 (2022) 5939–5948, https://doi.org/10.1016/j.aej.2021.11.021.

[33] Adnan, et al., Numerical analysis of magneto-radiated annular fin natural-convective heat transfer performance using advanced ternary nanofluid considering shape factors with heating source, Case Stud. Therm. Eng. 44 (Apr. 2023), 102825, https://doi.org/10.1016/j.csite.2023.102825.

[34] Y.-Q. Song, A. Hamid, T.-C. Sun, M. Ijaz Khan, S. Qayyum, R. Naveen Kumar, B.C. Prasannakumara, S.U. Khan, R. Chinram, Unsteady mixed convection flow of magneto-Williamson nanofluid due to stretched cylinder with significant non-uniform heat source/sink features, Alex. Eng. J. 61 (2022) 195–206, https://doi.org/10.1016/j.aej.2021.04.089.

[35] S. Ahmad, T. Hayat, A. Alsaedi, H. Ullah, F. Shah, Computational modeling and analysis for the effect of magnetic field on rotating stretched disk flow with heat transfer, Propulsion and Power Research 10 (2021) 48–57, https://doi.org/10.1016/j.jppr.2020.11.005.

[36] S.A. Shehzad, Z. Abbas, A. Rauf, Z. Abdelmalek, Dynamics of fluid flow through Soret-Dufour impacts subject to upward and downward motion of rotating disk, Int. Commun. Heat Mass Tran. 120 (2021), 105025, https://doi.org/10.1016/j.icheatmasstransfer.2020.105025.

[37] F. Mabood, J. Mackolil, B. Mahanthesh, A. Rauf, S.A. Shehzad, Dynamics of Sutterby fluid flow due to a spinning stretching disk with non-Fourier/Fick heat and mass flux models, Appl. Math. Mech.-Engl. Ed. 42 (2021) 1247–1258, https://doi.org/10.1007/s10483-021-2770-9.

[38] A. Rauf, A. Mushtaq, N.A. Shah, T. Botmart, Heat transfer and hybrid ferrofluid flow over a nonlinearly stretchable rotating disk under the influence of an alternating magnetic field, Sci. Rep. 12 (2022), 17548, https://doi.org/10.1038/s41598-022-21784-2.

[39] K. Sharma, N. Vijay, F. Mabood, I.A. Badruddin, Numerical simulation of heat and mass transfer in magnetic nanofluid flow by a rotating disk with variable fluid properties, Int. Commun. Heat Mass Tran. 133 (2022), 105977, https://doi.org/10.1016/j.icheatmasstransfer.2022.105977.

[40] M. Turkyilmazoglu, Flow and heat over a rotating disk subject to a uniform horizontal magnetic field, Z. Für Naturforschung A, Jan. (2022), https://doi.org/10.1515/zna-2021-0350.

[41] L. Xue, P. Keblinski, S.R. Phillpot, et al., Effect of liquid layering at the liquid–solid interface on thermal transport, Int. J. Heat Mass Tran. 47 (2004) 4277–4284.

[42] R.L. Hamilton, O.K. Crosser, Thermal conductivity of heterogeneous two-component systems, Industrial & Engineering chemistry fundamentals 1 (3) (1962) 187–191.

[43] S.M.S. Murshed, K.C. Leong, C. Yang, Investigations of thermal conductivity and viscosity of nanofluids, Int. J. Therm. Sci. 47 (2008) 560–568.

[44] K.C. Leong, C. Yang, S.M.S. Murshed, A model for the thermal conductivity of nanofluids – the effect of interfacial layer, J. Nanopart. Res. 8 (2006) 245–254.

[45] N. Acharya, F. Mabood, S.A. Shahzad, I.A. Badruddin, Hydrothermal variations of radiative nanofluid flow by the influence of nanoparticles diameter and nanolayer, Int. Commun. Heat Mass Tran. 130 (Jan. 2022), 105781, https://doi.org/10.1016/j.icheatmasstransfer.2021.105781.

[46] C.J. Yu, A.G. Richter, A. Datta, et al., Molecular layering in a liquid on a solid substrate: an X-ray reflectivity study, Physica B 283 (2000) 27–31.

[47] N. Ahmed, F. Saba, U. Khan, S.T. Mohyud-Din, E.-S.M. Sherif, I. Khan, Nonlinear thermal radiation and chemical reaction effects on a (Cu−CuO)/NaAlg hybrid nanofluid flow past a stretching curved surface, 12, Processes 7 (12) (Dec. 2019), https://doi.org/10.3390/pr7120962. Art..

[48] M. Žitňanský, L. Čaplovič, Effect of the thermomechanical treatment on the structure of titanium alloy Ti6Al4V, J. Mater. Process. Technol. 157 (158) (Dec. 2004) 643–649, https://doi.org/10.1016/j.jmatprotec.2004.07.151.

[49] N. Kelson, A. Desseaux, Note on porous rotating disk flow, ANZIAM J. 42 (Dec. 2000) C837–C855.

[50] N. Bachok, A. Ishak, I. Pop, Flow and heat transfer over a rotating porous disk in a nanofluid, Phys. B Condens. Matter 406 (9) (Apr. 2011) 1767–1772, https://doi.org/10.1016/j.physb.2011.02.024.

[51] M. Turkyilmazoglu, Nanofluid flow and heat transfer due to a rotating disk, Comput. Fluids 94 (May 2014) 139–146, https://doi.org/10.1016/j.compfluid.2014.02.009.